Submicrometer and Nanoscale Inorganic Particles Exploit the Actin Machinery To Be Propelled along Microvilli-like Structures into Alveolar Cells

Galya Orr,[†,*] David J. Panther,[†] Jaclyn L. Phillips,[†] Barbara J. Tarasevich,[‡] Alice Dohnalkova,[§] Dehong Hu,[†] Justin G. Teeguarden,[⊥] and Joel G. Pounds[∥]

[†]Chemical and Materials Sciences, [‡]Materials Sciences, [§]Environmental Molecular Sciences Laboratory, [⊥]Health Effects and Risk Sciences, and [∥]Biological Sciences, Pacific Northwest National Laboratory, Richland, Washington 99354

ABSTRACT The growing commerce in micro- and nanotechnology is expected to increase human exposure to submicrometer and nanoscale particles, including certain forms of amorphous silica. When inhaled, these particles are likely to reach the alveoli, where alveolar type II epithelial cells that are distinguished by apical microvilli are found. These cells play critical roles in the function of the alveoli and participate in the immune response to amorphous silica and other particles by releasing chemokines. The cellular interactions of the particles, which drive the cellular responses, are still unclear. Adverse effects of nanoparticles have been attributed, in part, to the unique properties of materials at the nanoscale. However, little is known about the cellular interactions of individual or small nanoparticle aggregates, mostly because of their tendency to agglomerate under experimental conditions. Here we investigate the interaction and internalization pathway of individual precipitated amorphous silica particles with specific surface properties and size, by following one particle at a time. We find that both 100 and 500 nm particles can take advantage of the actin turnover machinery within filopodia and microvilli-like structures to advance their way into alveolar type II epithelial cells. This pathway is strictly dependent on the positive surface charge of the particle and on the integrity of the actin filaments, unraveling the coupling of the particle with the intracellular environment across the cell membrane. The retrograde pathway brings a new mechanism by which positive surface charge supports particle recruitment, and potential subsequent toxicity, by polarized epithelial cells bearing microvilli.

KEYWORDS: nanoparticle · amorphous silica · alveolar · epithelial cell · microvilli

The environmental or occupational exposure of humans to submicrometer and nanoscale materials is expected to increase within the next few years as the result of the increasing use of such materials in industrial and medical applications.[1] Particles ranging from 1 nm to 1 μm that enter the respiratory tract can reach the alveoli at the distal ends of the respiratory tree,[2] where the alveolar type II epithelial cells that are distinguished by apical microvilli are found. These cells play critical roles in the function of the alveoli by secreting pulmonary surfactants that prevent the alveolar collapse with expiration,[3] and by differentiating into type I epithelial cells to replace damaged cells.[4] Importantly, alveolar type II epithelial cells have been shown to internalize certain particles ranging from a few micrometers to nanometers *in vivo*[5,6] and *in vitro*,[7–12] and they release chemokines[7–10,13,14] that can recruit inflammatory response cells to the affected site.[15] However, the cellular interactions and internalization pathways of the specific particles, which drive the cellular responses, are largely unknown. One of the potentially more extensive exposures to airborne particles results from the use of precipitated, pyrogenic, or gel amorphous silica particles in a wide range of industrial applications, including micro- and nanotechnologies. Animal studies have shown both adverse effects of these forms of amorphous silica particles on the pulmonary system[16] and toxicity to alveolar cells.[17–19] Alveolar type II epithelial cells that are exposed to submicrometer and nanoscale amorphous silica particles respond with an increase in the inflammatory gene expression and the release of chemokines,[20,21] but the underlying mechanism is still unclear.

The harmful effects of submicrometer and nanoscale particles have been attributed, in part, to the large surface-area-to-mass ratio, leading to increased reactivity and oxidative stress.[1,22,23] Under experimental conditions, however, where the localized concentration is high, nanomaterials tend to agglomerate, creating larger particles that might no longer carry the properties of the individual particle.[24–26] In addition, large particles can be easily detected and phagocytosed by the alveolar macrophages,[27] but it is currently thought that submicrometer and nanomaterials are able

See the accompanying Perspective by Hess and Tseng on p 390.

Ⓜ This paper contains enhanced objects available on the Internet at http://pubs.acs.org/journals/ancac3.

*Address correspondence to galya.orr@pnl.gov.

Received for review August 7, 2007 and accepted November 16, 2007.

Published online December 8, 2007. 10.1021/nn700149r CCC: $37.00

to escape the alveolar macrophages[26] and translocate across the epithelial cell layer into the circulatory system.[2,28–30] These observations support the idea that submicrometer and nanomaterials are presented to alveolar cells *in vivo* as individual particles or small submicrometer aggregates, which differ from the larger particles in their ability to interact with the cell. However, the cellular interactions and internalization pathways of individual submicrometer and nanoscale particles are largely unknown, including particle interactions with the alveolar type II epithelial cells. Particles can enter the living cell through diverse mechanisms,[31,32] which are strongly dependent on the size and surface properties of the particles.[34,35] Importantly, the surface properties also play a key role in particle toxicity, as was demonstrated with quartz particles.[33,36,37] For example, increasing the positive surface charge by amino groups directly increases particle uptake[35] and toxicity.[38]

Since the cellular interactions and internalization pathways of inhaled particles are going to drive the cellular response and ultimately the impact on the pulmonary system, we investigated the surface-dependent interaction of individual or small aggregates of submicrometer and nanoscale particles, as they are likely to be presented *in vivo*. We show that submicrometer and nanoscale precipitated amorphous silica particles are able to travel along filopodia and microvilli-like structures toward the cell body of cultured alveolar type II epithelial cells, where they can be internalized *via* small membrane vesicles. We find that this retrograde motion is strictly dependent on the positive surface charge of the particles, and on the retrograde actin flow[39,40] in these structures. Our observations indicate that positively charged particles bind negatively charged membrane molecules that, in turn, interact directly or indirectly with the actin filaments within filopodia and microvilli. As the retrograde flow of the filaments is generated in these structures, it leads to the retrograde motion of the membrane molecule and its bound particle. The retrograde pathway brings a new mechanism by which positive surface charge supports particle recruitment, and possibly subsequent toxicity, by polarized epithelial cells bearing microvilli.

RESULTS AND DISCUSSION

Positively Charged Submicrometer and Nanoscale Particles Reach the Cell Body by Traveling along Filopodia and Microvilli-like Structures. Alveolar type II epithelial cells play critical roles in the normal function of the alveoli by producing surfactants and replacing damaged type I epithelial cells.[3,4] These cells also participate in the immune response to certain particles and pathogens by releasing chemokines.[7–10,13–15] Investigating their interactions with specific particles could therefore aid in understanding their cellular response, and ultimately the impact of the particles on the function of the pulmonary system. Here we focus on a non-tumorigenic alveolar type II epithelial cell line (C10) that was derived from a normal lung of an adult mouse. This cell line has been shown to preserve its characteristic phenotype, including lamellar bodies and surface microvilli.[41,42] The microvilli are formed in our cultured cells (Supporting Information). The cells develop an overwhelming number of elongated structures that can be seen by light microscopy. Using scanning electron microscopy (SEM), we confirmed that these structures originate from the apical cell surface and are part of the microvillar system, which under our culture conditions consists of microvilli with different lengths ranging from 100 nm to several micrometers (Supporting Information). Although the large number and the typical size and distribution of the elongated microvilli seen in the SEM images correspond to the pattern we see under the light microscope, a definite distinction between these structures and other filopodia, which are fewer, thinner, and often longer, is not possible using light microscopy. We therefore refer to the shorter and stouter structures as microvilli-like structures and revert to the more general term, filopodia, to include all cytoplasmic extensions.

As discussed in the introduction, the initial interaction of submicrometer and nanoscale particles with the living cell is likely to occur *in vivo* at the level of individual particles or small submicrometer aggregates. The investigation of dynamic processes that underlie the interactions and internalization pathways of individual particles or small particle aggregates requires tools that gain insights into living cells with high spatial (nanometer) and temporal resolutions. While individual 500 nm particles can be detected and followed using time-lapse differential interference contrast (DIC) microscopy, another approach has to be taken for detecting individual 100 nm particles. Here we applied time-lapse total internal reflection fluorescence (TIRF) microscopy with single-molecule sensitivity to study the dynamic behavior of individual 100 nm particles in the living cell. Using DIC and TIRF microscopy at 200× magnification, we find that positively charged 100 and 500 nm precipitated amorphous silica particles can move along filopodia and microvilli-like structures toward the cell body. Figure 1 and the corresponding movie 1 demonstrate the retrograde motion of 500 nm particles, using a time series of DIC images that were acquired at 10 s intervals. Each particle is followed along the sequence of the images with a color-coded arrow that is added when the particle lands on the cell. Particles can dwell in their landing spot before starting to move, or become engaged in the motion immediately after landing. The particle marked by the red arrow demonstrates the immediate motion in the corresponding movie. By the end of the series, the particles are found by the cell body where other particles are already accumulated.

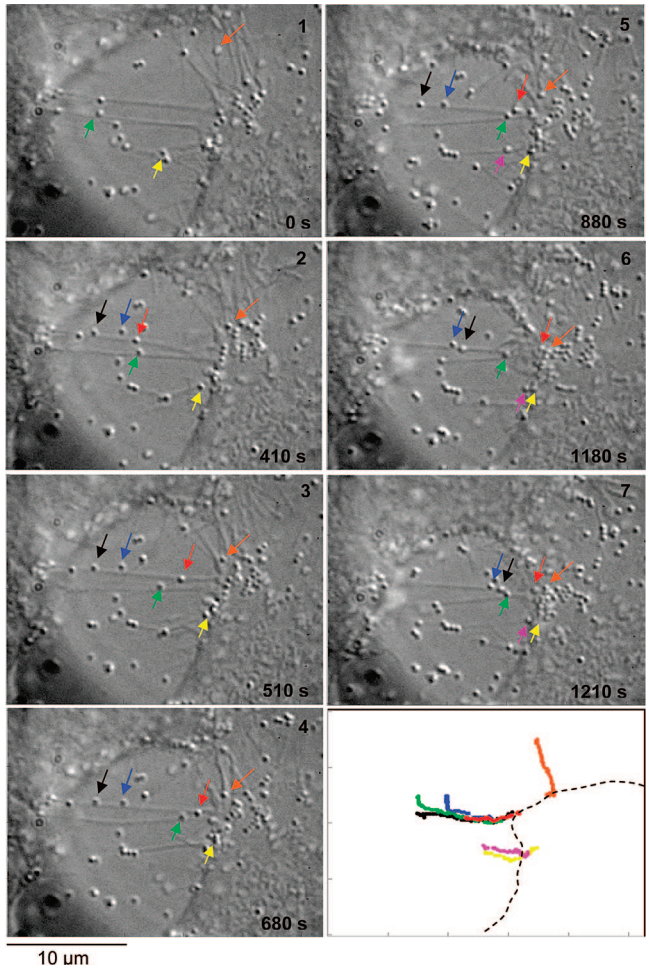

Figure 1. Positively charged submicrometer particles (≤500 nm) scroll along microvilli-like structures toward the cell body of alveolar type II epithelial cells growing in culture. A sequence of DIC images demonstrates the directed retrograde motion of 500 nm amorphous silica particles, which are positively charged by amino groups attached to their surface. The images are selected from a time series that was taken at 10 s intervals. The particles are indicated by color-coded arrows as they appear along the sequence. The cumulative time relative to the first image in the sequence is shown in the lower right corner of each image. Particle traces are generated by tracking the position of each particle from one image to the next in the series and are plotted in the last frame. The cell body from which the elongated structures originate is outlined with the dashed line. The traces show the directed motion of the particles and their accumulation by the cell-body membrane.

Ⓦ Movie 1 in AVI format shows the complete time series, played at 50 times the actual rate.

Figure 2 and the corresponding movie 2 demonstrate the retrograde motion of 100 nm particles, using single-molecule fluorescence techniques.[43] The images in Figure 2a are selected from a time series that was acquired using TIRF microscopy at 10 s intervals. The fluorescent spot that is indicated by the arrow in the first image is estimated to represent one nanoparticle or a cluster containing two nanoparticles. As described under Methods, the estimation is based on the intensity of the fluorescent spot and on the size of the spot, which is near the diffraction limit of the light (3×3 pixels). The particle travels along a microvillus-like structure that originates from the apical surface of the cell body, as shown in Figure 2b, where the trajectory of the nanoparticle is overlaid on the DIC image. Interestingly, the motion pattern of the nanoparticle, although clearly directed toward the cell body, includes both rearward and forward motions, as demonstrated in the corresponding movie.

Submicrometer and Nanoscale Particles Are Internalized *via* Membrane Vesicles That Enter the Lysosomal Pathway. As particles arrive closer to the cell body, they are often engulfed by lamellipodia that surround them and further bring them to the cell body, as demonstrated by the blue arrow in Figure 3 and the corresponding movie 3. Alternatively, particles can move up to the cell-body membrane, where they appear to be internalized at the site of their arrival, as demonstrated by the red arrow in the same figure and corresponding movie.

The internalization of the particles occurs through small membrane vesicles that bud from the plasma membrane, as shown in Figure 4a and the corresponding movie 4a. Using the fluorescent (Alexa 647) wheat germ agglutinin conjugate (WGA), which binds glycoproteins at the cell membrane, the origin of cytoplasmic vesicles can be traced to the plasma membrane. The co-localization of a 100 nm particle that is tagged with a fluorescent dye (Alexa 546) and a small membrane vesicle that originated from the plasma membrane, according to its fluorescence tagging by WGA, is shown in the merged image in Figure 4a. The nanoparticle and the vesicle move together in the cytoplasm, as seen in the movie of the merged images, further supporting their association. Using fluorescence-tagged transferrin, which is known to be internalized *via* clathrin-coated pits, the internalization of the particles *via* clathrin-dependent endocytosis can be determined. Figure 4b demonstrates the co-localization of transferrin and positively charged 100 nm particles within small vesicles, indicating that the particles can enter the cells *via* clathrin-mediated endocytosis. The internalized particles enter the lysosomal pathway, as determined using LysoTracker, a fluorescent indicator that is specific for acidic membrane organelles. Figure 4c and the corresponding movie 4c show the co-localization of fluorescent 500 nm particles and small acidic vesicles. Most of the particles are encased in the vesicles as individual or small clusters, as indicated by their size and fluorescence intensities. These acidic vesicles are fused with each other to form late en-

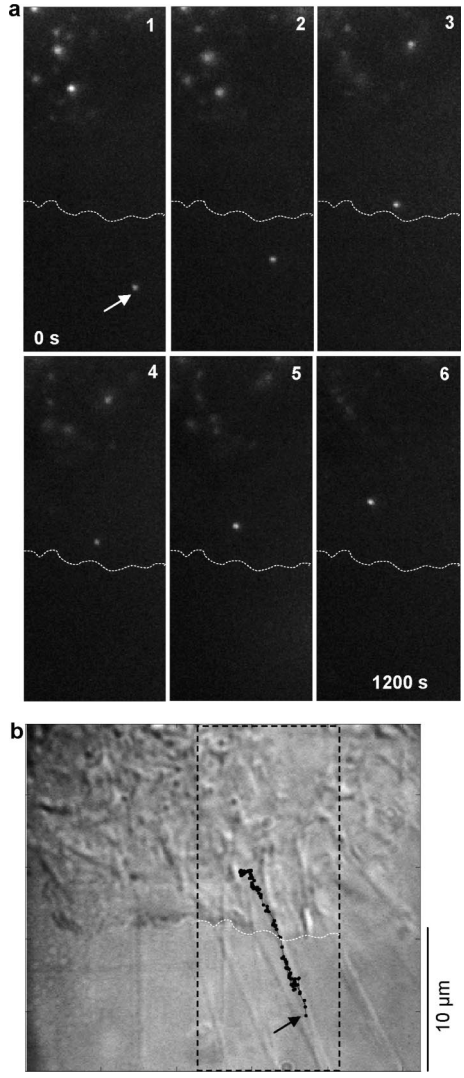

Figure 2. Positively charged nanoscale particles (≲100 nm) reach the cell body by traveling along microvilli-like structures in an irregular pattern that includes retrograde and anterograde motions. (a) Individual amorphous silica nanoparticles, positively charged with amino groups and tagged with an average of five fluorescent molecules (Alexa 546), are identified and tracked using single-molecule fluorescence microscopy. A sequence of fluorescence images demonstrates the retrograde motion of an individual 100 nm particle, which is marked by the arrow in the first image. The cell body is outlined by the dashed line. The fluorescent spots in the cell body represent internalized particles that become blurry as the focus follows the traveling particle up toward the apical cell surface. (b) The motion of the particle is traced along the time series and is plotted over the DIC image. The origin of the trace is indicated by the arrow, and the area shown in the fluorescence images is marked by the dashed lines.

Ⓦ Movie 2 in AVI format shows the complete time series at 50 times the actual rate.

dosomes and lysosomes. The interactions between the vesicles can be observed in the merged image in Figure 4c, where the larger vesicle, indicated by the arrow, is seen in contact with smaller vesicles. A dynamic view of the attachment and possible fusion of the vesicles can be seen in movie 4c. Since the green and red images are offset 5 s from each other, some of the merged images

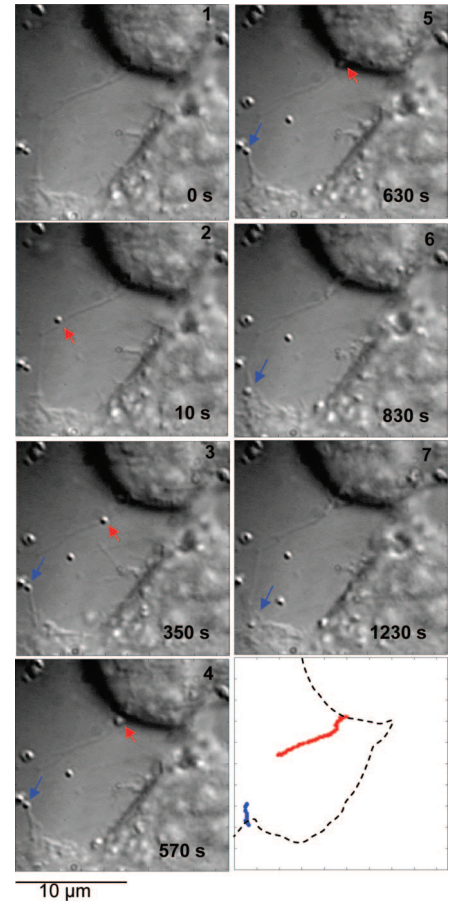

Figure 3. Particles that reach the cell body can be engulfed by extending lamellipodia or become internalized directly at the cell-body membrane. A sequence of DIC images shows internalization pathways of positively charged 500 nm amorphous silica particles. The cumulative time relative to the first image is indicated at the lower left corner of each image. The particle that is indicated by the red arrow scrolls up to the membrane of the cell body, where it seems to be internalized, while the particle indicated by the blue arrow is engulfed by a lamellipodium that reaches away from the cell body. The motion of the two particles is traced through the time series and plotted in the last frame relative to the outline of the cell body.

Ⓦ Movie 3 in AVI format shows the complete time series at 50 times the actual rate.

show a slight dissociation between the two dyes, resulting from the motion of the vesicle-bound particles during the delay between the two images.

Particle Surface Charge and Intact Actin Filaments Are Critical for the Retrograde Motion of the Particles. The observations above describe precipitated amorphous silica particles positively charged with amino groups attached to their surface. The addition of amino groups to particle surfaces has been used to create positive net charge, which has been shown to underlie the toxicity of certain particles and macromolecules.[38,44] While unmodified precipitated amorphous silica particles have a relatively strong negative net surface charge, with negative zeta potential $\zeta = -40$ mV at pH 7.4, the surface-aminated particles have a positive surface charge with $\zeta = +22$ mV at pH 7.4. Interestingly, we find that un-

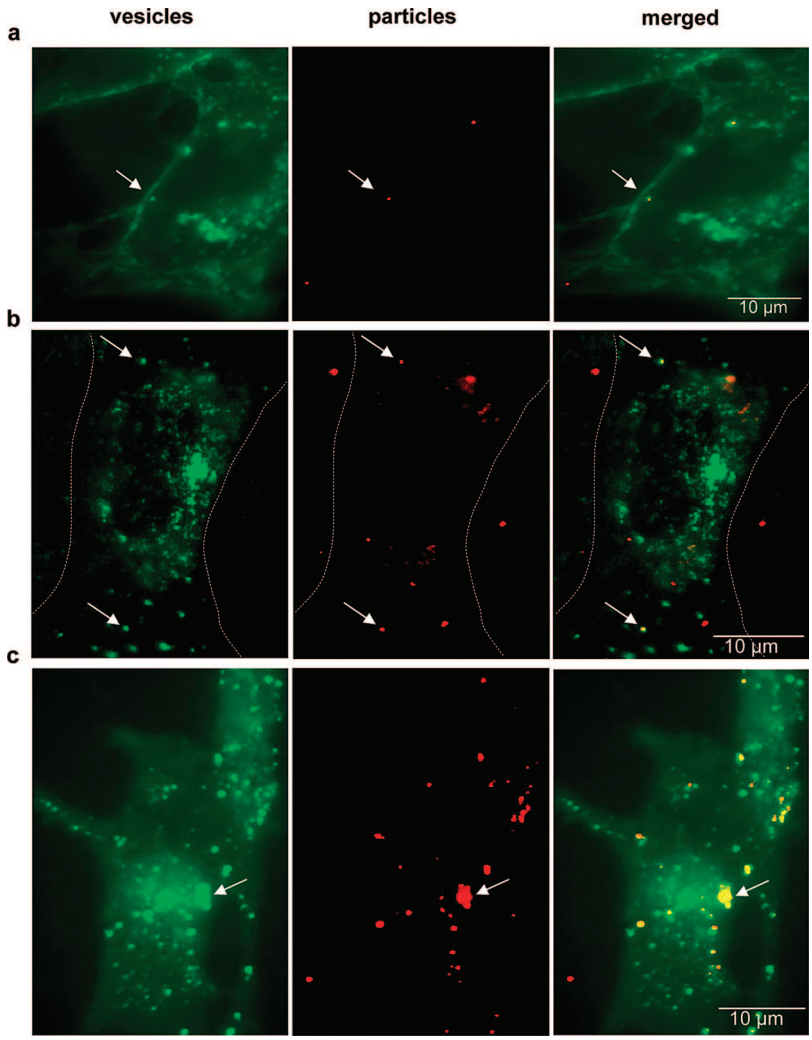

Figure 4. Positively charged submicrometer and nanoscale particles are internalized *via* membrane vesicles that can be mediated by clathrin, and reach the lysosomal pathway. (a) 100 nm particles that are tagged with an average of three fluorescent molecules (Alexa 546) are imaged using single-molecule fluorescence techniques. The fluorescent nanoparticle, indicated by the arrow in the middle image, is encased in a membrane vesicle that is labeled with a fluorescent probe of the plasma membrane (WGA—Alexa 647, left image). The co-localization of the nanoparticle and the vesicle is shown in the merged image on the right, where image pixels containing both red and green colors turn yellow. (b) 100 nm particles can be found co-localized with fluorescent transferrin, indicating that the particles can enter the cells *via* clathrin-dependent endocytosis. Transferrin molecules enter the cell (outlined by the dashed line) *via* vesicles that are budded from clathrin-coated pits, which are accumulate in the peri-nuclear region. Exposing cells to the particles and the fluorescent transferrin leads to the co-internalization of particles and transferrin molecules within one vesicle, as indicated by the arrows. (c) 500 nm particles that are tagged with the fluorescent dye (Alexa-546, middle image), co-localize with membrane vesicles that are tagged with LysoTracker (left image), a selective dye for acidic membrane organelles. The co-localization is shown by the yellow color in the merged image (right image). Most of the particles appear as individual or small aggregates that are tightly encased in small vesicles. The larger vesicle indicated by the arrow is likely to be a late endosome or a lysosome that is fused with smaller endosomes, as can be seen in movie 4c. The dissociation that is occasionally seen between the vesicles and the particles in the merged images in the movie is the result of the motion of the particle-containing vesicles during the 5 s offset between the green and the red images.

Ⓦ Movie 4a in AVI format shows the complete time series for panel a.

Ⓦ Movie 4c in AVI format shows the complete time series for panel c.

modified amorphous silica particles are unable to move along filopodia and microvilli-like structures. Although not all the positively charged particles that land on these structures eventually move, none of the unmodified particles that we observed on filopodia and microvilli-like structures moved from their landing spot (Figure 5a). To quantify these observations, we screened cells grown in 35 mm plates at 60–70% cell confluence over a 2 h time window, starting at the time of adding the particles to the culture plate. This time window allows us to capture the particles while in motion. An average of 18 positively charged 500 nm particles undergoing retrograde motion was found per plate during the 2 h time window (19 particles in plate 1, 15 particles in plate 2, and 21 particles in plate 3). The same experiment was repeated with unmodified par-

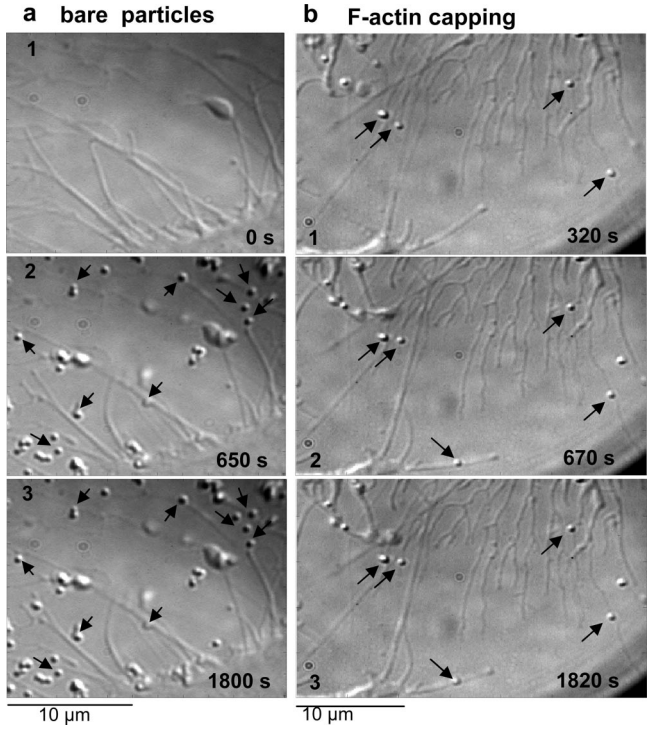

Figure 5. The directed motion of the particles along microvilli-like structures is strongly dependent on particle surface charge and intact actin filaments. (a) Unlike positively charged amorphous silica particles with amino groups on their surface, unmodified particles carry a negative net charge at pH 7.4. Unmodified particles that land on microvilli-like structures (arrows in the second image) do not move, as demonstrated by the particles being in the same position 19 min later (arrows in the third image). (b) Treating the cells with cytochalasin D, a toxin that caps the (+) end of actin filaments and eventually leads to depolymerization of the filaments, arrests the motion of the particles along filopodia and microvilli-like structures. The effect of the toxin is demonstrated by the position of the particles, which stays the same over time.

ticles. While particles landed on filopodia and microvilli-like structures, none of them moved from their original position (analysis of variance (ANOVA): $F = 7.7$, $P = 0.0004$). These observations indicate that the retrograde motion of the particles is dependent on electrostatic interactions between negatively charged molecules in the plasma membrane and the positively charged surface of the particles.

Directed motion of molecules and organelles in the cellular environment often relies on cytoskeletal elements. Filopodia and microvilli are rich with actin filaments that could play a role in the retrograde motion of the particles. To explore a role for actin filaments in this motion, we used toxins that interfere with the integrity of the filaments. We found that latrunculin, a highly potent drug that leads to depolymerization of the filaments, degrades the filopodia and microvilli-like structure within minutes. We therefore used cytochalasin D, a more moderate toxin that caps the (+) end of the filaments and prevents the addition of new monomers, leading to depolymerization of the filaments over time. Figure 5b shows cytochalasin-treated filopodia and microvilli-like structures. Most of the structures lost their apparent firmness and became flat, probably as the result of filament degradation. However, some of the thicker microvilli-like structures, such as the one at the bottom of the image, kept their general morphology. In spite of the relatively well preserved morphology, positively charged 500 nm particles that land on these structures do not move, as demonstrated by their unchanged position over more than 25 min. Under control experiments, we observed an average of 17 particles undergoing retrograde motion during the 2 h time window described earlier (16 particles in plate 1, 20 particles in plate 2, and 15 particles in plate 3). An average of 1 particle undergoing retrograde motion was observed in plates treated with cytochalasin D (0 particles in plate 1, 2 particles in plate 2, and 1 particle in plate 3). ANOVA showed a significant difference ($F = 7.7$, $P = 0.0006$) between the control and drug-treated plates. These observations indicate that the integrity of the actin filaments is critical to the motion of the particles.

To investigate the possibility that the retrograde motion of the particles is powered by adenosine triphosphatase (ATP)-dependent mechanisms, we incubated the cells in a glucose-free medium with 10 mM sodium azide and 6 mM 2-deoxy-D-glucose to deplete ATP. However, no significant difference was observed in the number of particles undergoing retrograde motion under control and ATP-depleting conditions. An average of 16 positively charged 500 nm particles undergoing retrograde motion was observed under control conditions (18 particles in plate 1, 15 particles in plate 2, and 14 particles in plate 3), and an average of 13 particles was observed under ATP-depleting conditions (ANOVA: $F = 7.7$, $P = 0.12$). These observations indicate that the retrograde motion of the particles can occur without the contribution of myosin or other ATP-dependent motor proteins.

GFP—Actin Clusters in Filopodia and Microvilli-like Structures Move toward the Cell Body in the Same Retrograde Pattern and Rate as the Particles. Actin filaments at the leading edge of many cells undergo a continuous cycle of assembly at their distal barbed end and disassembly at their proximal end. This treadmilling underlies a process termed "actin retrograde flow", which plays an important role in cell migration or axonal growth cone guidance, among other cellular processes.[39] The mechanism underlying the actin retrograde flow has been studied intensively in the leading edge of the growth cone, but less is known about this process in microvilli. Previously, it was thought that both actin treadmilling and certain myosin molecules power the flow. However, recent observations demonstrate that the retrograde flow of actin in the peripheral domain of the axonal growth cone can be driven only by actin treadmilling.[40] The flow of actin has been suggested to underlie the retrograde motion of membrane receptors when they are activated by their ligands.[45,46] To explore the possibility that the retrograde flow of actin within the filopodia

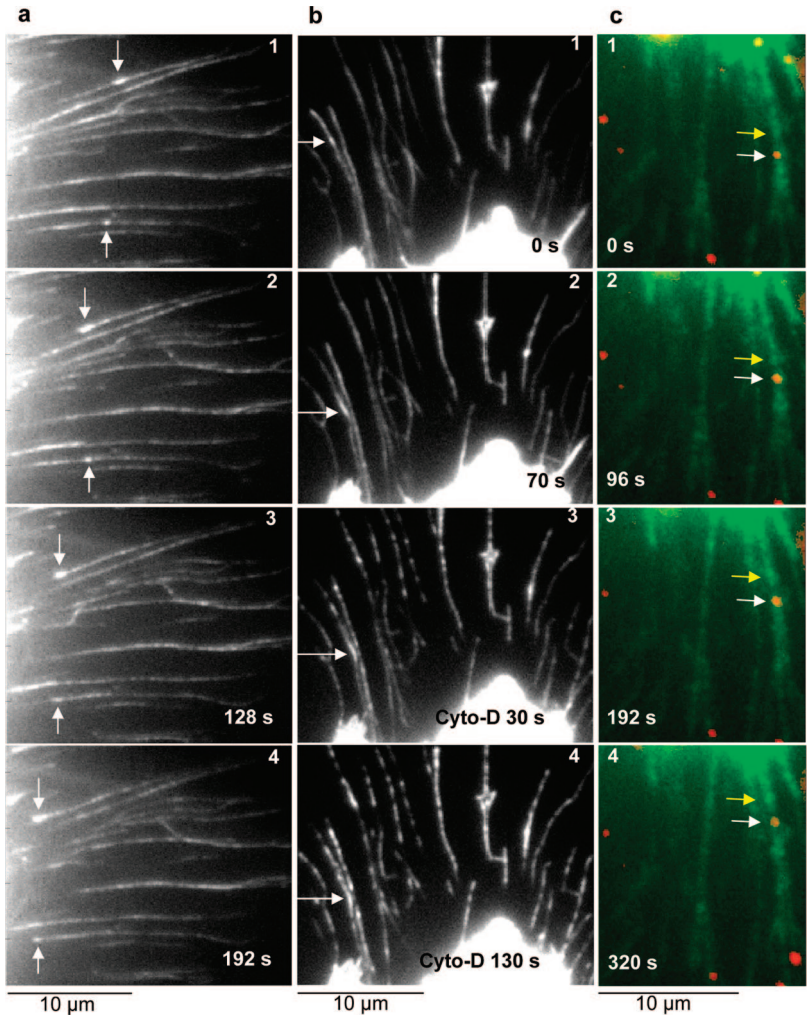

Figure 6. A retrograde actin flow is detected in filopodia and microvilli-like structures using GFP−actin, and just like the retrograde motion of the particles, this retrograde flow is inhibited by cytochalasin D. (a) The transfection of alveolar type II epithelial cells with GFP−actin leads to fluorescent filopodia and microvilli-like structures that often contain small fluorescent clusters, which are distinguished from the diffused signal. Following the clusters over time reveals their retrograde motion toward the cell body. The images are selected from a time series that was taken at 32 s intervals. Two clusters that are marked by arrows move toward the cell-body edge on the left side of the images. The cumulative time relative to the first image is indicated in the lower right corners. (b) Treating transfected cells with cytochalasin D leads to fragmented filaments and the arrest of the actin flow, as clearly demonstrated in the corresponding movie 6b. The two upper images were taken before adding cytochalasin D, showing the retrograde motion of the cluster indicated by the arrow. The two lower images were taken after addition of the drug, where the cumulative time relative to the time of applying the drug is shown in the lower right corner. These images show that the cluster stopped moving after addition of the drug, and the filaments became fragmented. (c) Images of 500 nm fluorescent particles are overlaid on images of a cell expressing GFP−actin. The white and yellow arrows point to an actin cluster and a particle, respectively. The images demonstrate that the particle and the actin cluster move together toward the edge of the cell body at the top of the image.

Ⓦ Movie 6a in AVI format shows the time series for panel a at 107 times the actual rate.

Ⓦ Movie 6b in AVI format shows the complete time series for panel b at 107 times the actual rate.

and microvilli-like structures powers the retrograde motion of the particles, we transfected the cells with the green fluorescent protein (GFP) chimera of actin. Transfected cells show fluorescent filopodia and microvilli-like structures, where distinct fluorescent clusters can occasionally be identified. These clusters can undergo a retrograde motion, as demonstrated in Figure 6a and the corresponding movie 6a. The arrows in the images point to a couple of clusters that move toward the edge of the cell body on the left side of the image.

When transfected cells are treated with cytochalasin D, the actin flow is halted and the filaments become fragmented or depolymerized over time, as shown in Figure 6b and the corresponding movie 6b. The inhibition of actin flow by the drug is in agreement with the current understanding of the mechanism underlying this motion, where actin treadmilling powers the flow. A series of overlaid images of a 500 nm particle and a cell expressing GFP−actin is shown in Figure 6c. The white and yellow arrows point to the particle and the actin

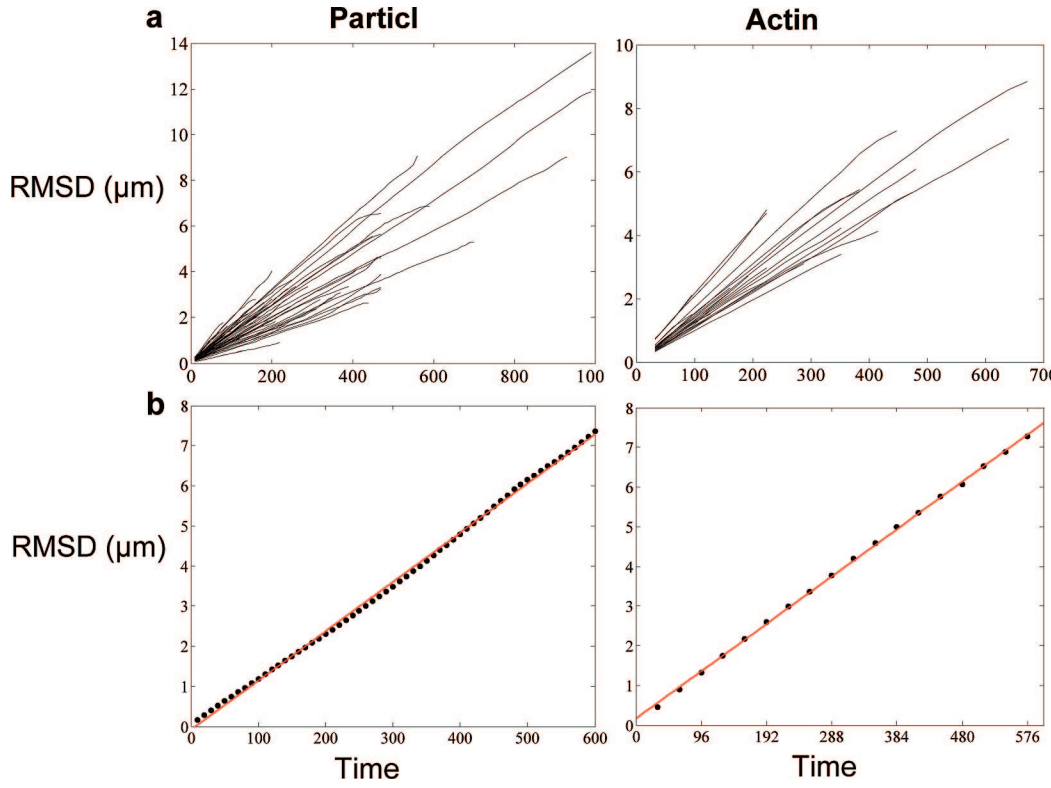

Figure 7. The retrograde flow of actin clusters in filopodia and the retrograde motion of the particles along these structures occur at the same rate. (a) Root-mean-square displacements (rmsd) of 60 particles (left) and 25 actin clusters (right) are plotted over the time intervals, demonstrating the directed motion of the particles and the actin clusters. (b) The averaged rmsd for the particles (left) and the actin clusters (right) are fitted with a linear line (red), and the average velocities are estimated from the slope of the line, showing 12.3 nm/s for the particles and 12.4 nm/s for the actin clusters.

cluster, respectively, which move together toward the cell body at the top of the image.

To verify that the clusters and particles move at the same rate, the motion rates of 60 particles and 25 actin clusters were quantified. Figure 7a shows root-mean-square displacements (rmsd) of the particles (left) and the actin clusters (right). By fitting a linear line to the averaged rmsd of the particles (Figure 7b, left) and the actin clusters (Figure 7b right), the estimated velocities can be calculated, showing 12.3 and 12.4 nm/s for the particles and the clusters, respectively. These values were verified by calculating velocities of each of the 60 particles and the 25 actin clusters, using the first and last positions in their respective trajectory. The averaged values show 11.6 $\pm$ 3.8 and 13.9 $\pm$ 3.4 nm/s for the particles and the clusters, respectively. The values indicate that the retrograde flow of actin and the retrograde motion of the particles occur at the same rate. Together with the observation that capping the (+) end of the filaments arrests the retrograde flow of actin and the retrograde motion of the particles, these values indicate that the retrograde motion of the filaments underlies the retrograde motion of the particles.

The Retrograde Motion Unravels the Coupling of Inorganic Submicrometer and Nanomaterials with the Intracellular Environment across the Cell Membrane. As illustrated in Figure 8, our observations indicate that positively charged particles bind a negatively charged membrane molecule that, in turn, interacts directly or indirectly with the actin filaments within filopodia and microvilli. As actin monomers are added to the filaments at the distal tip of these structures, a retrograde motion of the filaments is generated, leading to the retrograde motion of the membrane molecule and its bound particle. A retrograde movement of specific membrane receptors, including their specific ligands and ligand-coated pathogens, has been shown or inferred,[45–49] but these highly specific and evolved interactions between receptors and their ligands cannot account for the nonspecific interaction of a ligand-free inorganic material with the cell membrane. Studies of cationic polymeric particles

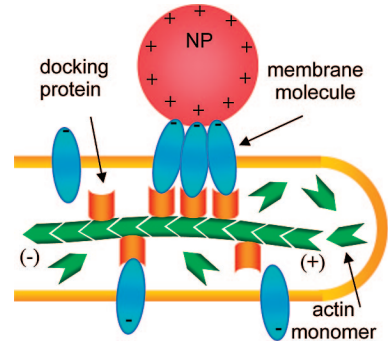

Figure 8. Illustration of the emerging mechanism underlying the retrograde recruitment pathway of positively charged submicrometer and nanoscale inorganic particles. See text for discussion.

or liposomes developed for DNA delivery suggest electrostatic interactions between the positively charged particle and negatively charged anionic proteoglycans, such as heparan sulfate or chondroitin sulfate proteoglycans.[50] Certain members of this family are transmembrane proteoglycans[50] that indirectly interact with actin filaments.[51] These molecules might be the link between the nanoparticles and the actin filaments, a possibility that we are currently investigating.

The Retrograde Pathway Brings a New Mechanism by Which Positive Surface Charge Supports Particle Recruitment and Potential Subsequent Toxicity. Inorganic or polymeric particles have been found tightly associated with microvilli,[10,35] but the consequence of this association was not understood. Using SEM combined with electron dispersive spectroscopy (EDS), we also observed these tight associations between positively charged particles and the base of microvilli on the apical surface of our cells, as demonstrated in Figure 9. These associations were more readily observed near the cell body after 1–2 h of incubation with the particles. Our findings provide a new insight into this association. The retrograde recruitment pathway that we describe is only one pathway by which the particles can gain access into the cytoplasm of these cells. We observed both 100 and 500 nm positively charged particles within alveolar type II epithelial cells treated with cytochalasin D, although to a lesser extent than their internalization by nontreated cells (observations not shown). The attenuated internalization of the particles could result from interfering with the endocytic process itself,[52,53] and with the retrograde recruitment of the particles. Coating submicrometer polystyrene particles with amino groups to increase their positive surface charge has turned relatively nontoxic particles into particles that are highly toxic to phagocytic cells in culture.[38] Together with the observation that the internalization of polymeric particles in primary stem cells and several cell lines in culture is increased with the increase in the amino groups on their surface,[35] the observed increase in toxicity could result from the increase in particle internalization. The positive charge densities of macromolecules has been thought to facilitate their interaction with the cell membrane and account for the increase in their toxicity that was observed with increases in their positive charges.[44,38] Our observations bring a new mechanism by which positive surface charge could lead to increased particle internalization and potential toxicity in polarized epithelial cells bearing microvilli.

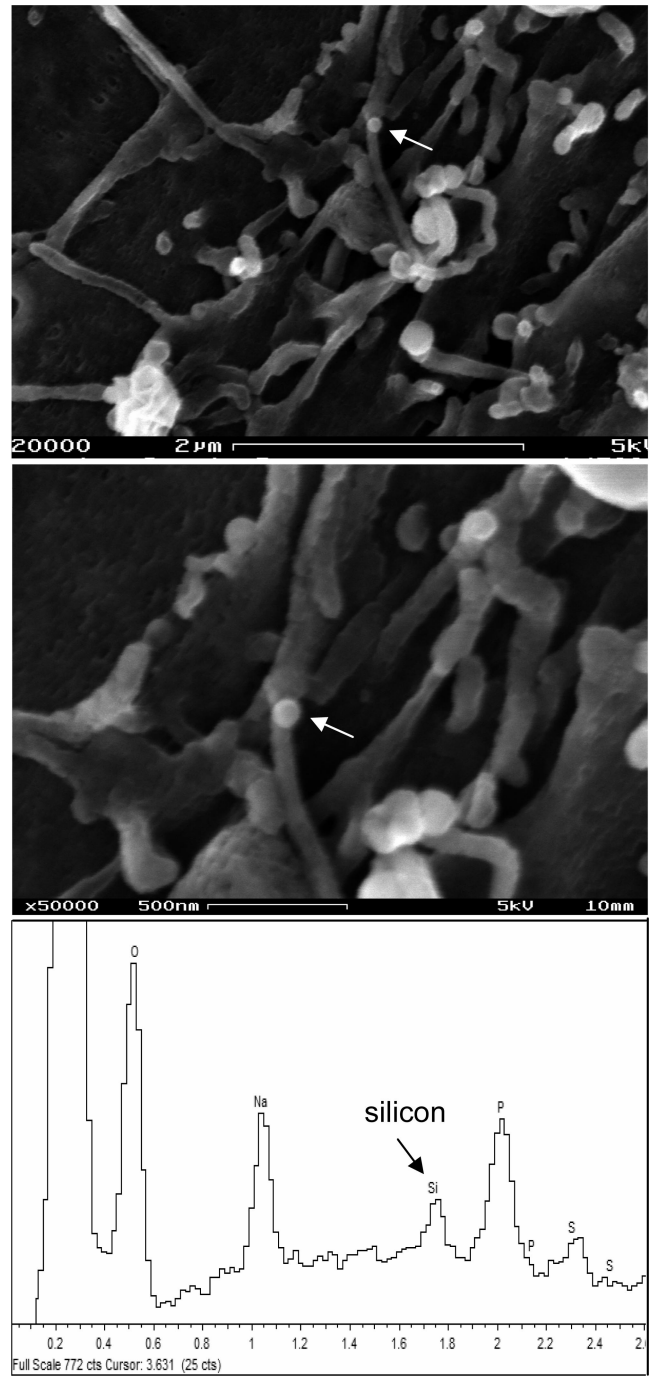

Figure 9. Positively charged 100 nm amorphous silica particles are found at the base of microvilli in the apical surface of the cells. Using EDS to identify the elemental composition of structures seen by SEM, it was possible to distinguish between 100 nm amorphous silica nanoparticles and the smaller microvilli found at the apical surface, which are often the size and shape as these particles. The amorphous silica nanoparticle indicated by the arrow in the upper image (lower magnification) and the lower image (higher magnification) was identified by the silicon peak in the elemental spectrum.

METHODS

Cell Culture, Transfection, Drugs, and Probes. The alveolar type II epithelial cell line, C10, was used in these studies. C10 is a nontumorigenic cell line that was derived from normal adult mouse lung and has been shown to preserve its characteristic lamellar bodies and microvilli[41,42] (Supporting Information). The cells were grown in CMRL 1066 growth medium, supplemented with 10% FBS, 2 mM glutamine, 100 U/mL penicillin, and 100 µg/mL streptomycin, all from Invitrogen (Carlsbad, CA). Cells were

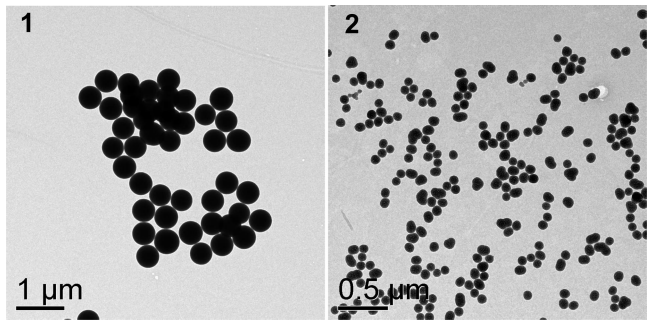

Figure 10. Transmission electron micrographs of the 500 nm (panel 1) and 100 nm (panel 2) precipitated amorphous silica particles used in our experiments. The images indicate that the particles are colloidal and disperse. The average diameter, found by measuring 50 particles per size, is 462 ± 20.5 and 92.2 ± 13.2 nm for the larger and smaller particles, respectively.

grown in 35 mm glass coverslip bottom plates (WPI, Sarasota, FL) and imaged in physiological buffer (162 mM NaCl, 2.5 mM KCl, 1.0 mM $CaCl_2$, 10 mM glucose, 10 mM HEPES, pH 7.4) containing 1% BSA (Fisher) to avoid particle clustering. For measuring actin flow, cells were transfected with the plasmid for GFP−actin, kindly provided by Stefano Vicini (Georgetown University). Transfection was done using LipofectAmine (Invitrogen) in the growth medium with no serum, and the cells were studied 24–48 h after transfection. To cap the (+) end and depolymerize F-actin, cells were incubated with 5 μM cytochalasin D (Sigma, St. Louis, MO) in their normal growth medium for 20 min and washed before imaging. ATP depletion was done by incubating the cells in glucose-free DMEM (Invitrogen) supplemented with 10 mM sodium azide and 6 mM 2-deoxy-D-glucose. The cells were pre-incubated with the depletion medium for 20–30 min before addition of the particles, and were observed while in the depletion medium. Wheat germ agglutinin−Alexa 647 (WGA−Alexa 647, Molecular Probes/Invitrogen) was used to tag the plasma membrane. Cells were imaged while being exposed to the probe (20 μg/mL). Fluorescent transferrin (Molecular Probes/Invitrogen) was used to detect clathrin-dependent endocytosis. Cells were incubated with transferrin (10 μg/ml) and the particles for 30–60 min at 37 °C and washed before imaging. LysoTracker (Molecular Probes/Invitrogen) was used to tag acidic vesicles and organelles. Cells were incubated with the probe (1 nM) and the particles for 30–60 min at 37 °C and washed before imaging.

Particle Characterization. Amorphous silica particles of 100 and 500 nm size were obtained commercially as unmodified bare particles (Polysciences, Inc.) or particles modified with amine groups (Corpuscular, Inc., Cold Spring, NY). The amination of the particles was also done in our laboratory as described below. The particles were synthesized by solution precipitation methods to form spherical disperse particles. The precipitation methods lead to silica particles that are negatively charged, preventing hard aggregate formation during precipitation and allowing the formation of disperse particles. Zeta potentiometry of the unmodified particles at pH 7.4 resulted in $\zeta = -40$ mV. Particles modified with amine groups had $\zeta = +20$ mV at pH 7.4. The solution precipitation methods, which occur at ambient or relatively low temperatures, result in the formation of amorphous silica particles. The formation of amorphous particles was confirmed for our particles by X-ray and electron diffraction. The colloidal disperse nature of the particles was confirmed using transmission electron microscopy (TEM, Figure 10). The size distribution was determined from TEM images of 50 particles per size group, showing 462 ± 20.5 and 92.2 ± 13.2 nm for the larger and smaller particles, respectively.

Particles were sonicated by placing the tube with the particle solution in a bath sonicator before being applied to the cells. Our experimental approach allowed the identification of individual particles by either DIC (500 nm) or fluorescence (100 nm) microscopy. Individual 500 nm particles were pursued. When studying 100 nm particles, individual or small aggregates containing two or three nanoparticles were pursued. The estimation of the number of nanoparticles found within a fluorescent spot is described below. Particles were added to the cells at concentrations that were adjusted theoretically[54] and experimentally to give an exposure in the order of 10–300 particles per cell, as estimated by DIC and fluorescence imaging (0.5 μg/mL for 500 nm particles and 0.1 μg/mL for 100 nm particles, in a 1 mL final volume over a 35 mm plate). Identical concentrations were added when comparing between treatments.

Surface Amination and Fluorescence Tagging of the Particles. Particles were aminated either commercially or in our laboratory with (3-aminopropyl)triethoxysilane (APTES, Sigma-Aldrich, St. Louis, MO). The 500 nm bare particles were reacted with APTES in toluene at 80 °C for 6 h. APTES solution amounts were 1.5 times the amount that would give monolayer coverage. After reaction, the particles were separated by centrifugation and washed repeatedly in toluene and ethanol. Commercial 100 nm aminated particles were separated from aqueous suspension by adding a few drops of 1 M HCl to the suspension to reduce the pH to ~2–3 and centrifuging the particles. The particles were then repeatedly washed in dimethylformamide (DMF, Sigma-Aldrich). The 100 and 500 nm particles were dye-labeled by reacting the succinimidyl ester-conjugated Alexa Fluor 546 (Molecular Probes/Invistrogen) directly with amine groups on the particles. The particles were placed into DMF at ~25 mg/mL and dispersed by ultrasonication, and various amounts of the dye in DMF were added to the suspensions. Reaction occurred at room temperature for 2–3 h under rotation. After reaction, the particles were separated by centrifugation and repeatedly washed in DMF, ethanol, and water. Unmodified particles were tagged with fluorescent molecules by reacting silanated dye with hydroxyl groups on the silica surface. The dye was silanated by reacting the dye (50 μg/50 μL ofDMF) with 50 μL of a 2 mM APTES solution in DMF for 2 h at room temperature under rotation. Silica particles were hydrated in a humidity chamber for 1–2 h and placed into anhydrous toluene (at ~5 mg/mL) concentration. The silanated dye solution was diluted in 1 mL of DMF, and various amounts of dye solution were added. The suspensions were heated to 90 °C for 6 h and cooled, and the particles were separated by centrifugation. The particles were repeatedly washed in toluene and ethanol and then dried by lyophilization. The dye concentrations were controlled to achieve low coverage of dye molecules per particle. The number of dye molecules per particle was estimated as described below, and the solution concentrations were adjusted accordingly to achieve an average of three dye molecules per particle.

Fluorescence and DIC Microscopy. A total internal reflection (TIRF) fluorescence laser microscope (Axiovert 200, Zeiss) equipped with a 100× oil-immersion objective (Plan-Apochromat, N.A. = 1.4, Zeiss) and a 2× relay lens in the emission path to the CCD camera was used. The overall magnification was 200×, leading to 100 nm per image pixel. A green laser (Nd:YAG Verdi V-10, Coherent) was used to excite the particles (Alexa 546) at 532 nm, a blue laser (Innova, Coherent) was used to excite GFP−actin at 488 nm, and a red laser (dye laser CR-599, Coherent) was used to excite WGA−Alexa-647 at 632 nm. The lasers were coupled by a fiber coupler to the TIRF module, and the illumination intensity was set to 8 mW at the input to the objective. Shutters, controlled by the CCD controller, were set in front of the laser beams to produce 100 ms laser exposures. Dichroic mirrors (Chroma Technology) were set to split the emissions of GFP and Alexa 546 at 550 nm, and to split the emissions of Alexa 546 and Alexa 647 at 600 nm. Fluorescence images were acquired by a back-illuminated nitrogen-cooled CCD camera (Spec-10 1340×700, Roper Scientific) with 90% quantum efficiency and single-molecule sensitivity. It is estimated that one intensity count in the CCD image corresponds to two detected photons. DIC images were taken at 200× magnification, using the above CCD camera.

Detecting Individual Nanoparticles Using Single-Molecule Fluorescence Imaging. The particles were tagged with 1–5 fluorescent molecules, which allowed the application of single-molecule fluorescence techniques for detecting individual nanoparticles and estimating the number of nanoparticles within a fluorescent spot. The single-molecule fluorescence technique was described earlier in detail.[43] Briefly, three criteria were used to identify individual fluorophores. (1) The size of the fluorescent spot should

be at the diffraction limit, which is about half of the excitation wavelength, or 3×3 pixels (300 nm^2), under our experimental conditions. (2) The fluorescent spot blinks and photobleaches in one discrete step. (3) The intensity of the fluorescent spot falls within the intensity distribution of single fluorophores, diluted to picomolar concentrations in agarose, and imaged after being spin-coated on a glass slide. The expected fluorescence intensity of a single Alexa 546 molecule under our specific experimental conditions using TIRF microscopy is 136 ± 70 counts per 3×3 pixels. This value was determined by the peak of the fluorescence intensity distribution that was generated by imaging hundreds of individual dye molecules. The intensity distribution of individual 100 nm fluorescent particles, diluted in agarose and spin-coated on a glass slide, peaks at 367 ± 175 counts. These values indicate that the nanoparticles were tagged on average with ~3 dye molecules per particle. To ensure that our studies are focused on the cellular interactions of individual nanoparticles or small, nanoscale aggregates, we used the diffraction limit size (3×3 pixels) and the expected fluorescence intensity of 3 dye molecules (~400 counts) to detect individual fluorescent particles or estimate the number of particles within a small aggregate.

Calculating the Position of Individual Particles. Although the spatial resolution of fluorescence imaging is limited by the diffraction limit of light, we[43] have developed analytical methods that allow us to study the spatial behavior of individual fluorescence-tagged molecules or particles with 20–40 nm resolution by following the center of the fluorescent spot. The center of individual fluorescent spots was determined by a Gaussian mask algorithm using iterations of the following equation:

$$x = \left(\sum iS_{ij}G_{ij}\right) / \left(\sum S_{ij}G_{ij}\right) \quad (1)$$

S_{ij} is the photon counts at pixel (i,j), and G_{ij} is a two-dimensional (2D) Gaussian function with a peak x and a full width at half-maximum (fwhm) that equals 300 nm, which is given by the point-spread function of the microscope. Because G_{ij} depends on x, the calculation of x is iterated until x is converged. The accuracy of the Gaussian mask algorithm was tested both experimentally and by mathematical simulations, which indicated that the accuracy of the fitting is within 20–40 nm. The fluorescence intensity of each spot was calculated by the summation of 3×3 pixels area, which is at the diffraction limit size. For a 2D Gaussian profile with 300 nm at fwhm, 60% of the fluorescence intensity falls within the 3×3 pixels (100 nm/pixel). The center of the particles that were imaged by DIC microscopy is based on the approach described earlier[55] and on the observation that a DIC image of each particle consists of a pair of black and white peaks. Briefly, a typical 21×21 pixel image of a sphere is chosen as a "kernel" segment (K). The 2D cross-correlation $C(x,y)$ of every DIC image data, $I(x,y)$ and K, is then calculated. In the image of $C(x,y)$, only one Gaussian-shape positive peak appears for each particle. The maximum value in that peak is the center of the particle.

Calculating Root-Mean-Square Displacement and Velocity. The trajectories of individual particles were acquired by following the center of the particles, which were calculated as described above, from one frame to the next in the series. The trajectories of actin clusters were done by following the x,y coordinates of the leading edge of the clusters. These trajectories were used to compute the following values. The rmsd values of individual particles are defined by eq 2,

$$\mathrm{RMSD} = \sqrt{\langle r(t)^2 \rangle} \quad (2)$$

where r is the distance between steps, in time t. The velocity of individual particles and actin clusters was calculated using eq 3,

$$v = \Delta d/t \quad (3)$$

where Δd is the distance between the first and the last positions in the trajectory, and t is the time it takes to reach the last position.

Scanning Electron Microscopy. SEM was performed using a LEO 982 field-emission scanning electron microscope (FE SEM) operated at 3 keV. Electron dispersive spectroscopy instrumentation (Oxford) was used for the elemental identification of the nanoparticle material. SEM sample preparation included the conventional fixation in 2.5% glutaraldehyde, followed by three washes in phosphate buffer and gradual dehydration in ethanol series. Samples were further processed by critical point drying, sputtered with a very thin carbon layer, and observed at 3 keV in the SEM.

Acknowledgment. We thank B. Arey for his help with SEM and EDS. The research was supported by the Environmental Biomarkers Initiative at the Pacific Northwest National Laboratory (PNNL), operated by Battelle for the U.S. Department of Energy, and by the EPA's Science to Achieve Results (STAR) grant RD833338. The work was performed in the Environmental Molecular Sciences Laboratory, a national scientific user facility sponsored by DOE-OBER and located at PNNL.

Supporting Information Available: Scanning electron micrographs of alveolar type II epithelial (C10) cells grown in culture, showing the formation of microvilli at the apical membrane of the cells. In panel a, the microvilli are formed with different lengths ranging from 100 nm to several micrometers; in panel b, farther away from the center of the cell, the microvilli become more sparse and the number of elongated microvilli is increased; and in panel c, closer to the edge of the cell, some of the elongated microvilli (indicated by white arrows) land on the glass bottom of the dish. This information is available free of charge *via* the Internet at http://pubs.acs.org.

REFERENCES AND NOTES

1 Nel, A.; Xia, T.; Madler, L.; Li, N. Toxic Potential of Materials at the Nanolevel. *Science* **2006**, *311*, 622–627.
2 Oberdorster, G.; Oberdorster, E.; Oberdorster, J. Nanotoxicology: an Emerging Discipline Evolving from Studies of Ultrafine Particles. *Environ. Health Perspect.* **2005**, *113*, 823–839.
3 Weaver, T. E.; Whitsett, J. A. Function and Regulation of Expression of Pulmonary Surfactant-associated Proteins. *Biochem. J.* **1991**, *273* (Pt. 2), 249–264.
4 Kinnard, W. V.; Tuder, R.; Papst, P.; Fisher, J. H. Regulation of Alveolar Type II Cell Differentiation and Proliferation in Adult Rat Lung Explants. *Am. J. Respir. Cell Mol. Biol.* **1994**, *11*, 416–425.
5 Corrin, B. Phagocytic Potential of Pulmonary Alveolar Epithelium with Particular Reference to Surfactant Metabolism. *Thorax* **1970**, *25*, 110–115.
6 Kato, T.; Yashiro, T.; Murata, Y.; Herbert, D. C.; Oshikawa, K.; Bando, M.; Ohno, S.; Sugiyama, Y. Evidence that Exogenous Substances Can be Phagocytized by Alveolar Epithelial Cells and Transported into Blood Capillaries. *Cell Tissue Res.* **2003**, *311*, 47–51.
7 Stringer, B.; Imrich, A.; Kobzik, L. Lung Epithelial Cell (A549) Interaction with Unopsonized Environmental Particulates: Quantitation of Particle-Specific Binding and IL-8 Production. *Exp. Lung. Res.* **1996**, *22*, 495–508.
8 Juvin, P.; Fournier, T.; Boland, S.; Soler, P.; Marano, F.; Desmonts, J. M.; Aubier, M. Diesel Particles are Taken up by Alveolar Type II Tumor Cells and Alter Cytokines Secretion. *Arch. Environ. Health* **2002**, *57*, 53–60.
9 Calcabrini, A.; Meschini, S.; Marra, M.; Falzano, L.; Colone, M.; De Berardis, B.; Paoletti, L.; Arancia, G.; Fiorentini, C. Fine Environmental Particulate Engenders Alterations in Human Lung Epithelial A549 Cells. *Environ. Res.* **2004**, *95*, 82–91.
10 Ovrevik, J.; Refsnes, M.; Namork, E.; Becher, R.; Sandnes, D.; Schwarze, P. E.; Lag, M. Mechanisms of Silica-Induced IL-8 Release from A549 Cells: Initial Kinase-Activation does not Require EGFR Activation or Particle Uptake. *Toxicology* **2006**, *227*, 105–116.
11 Stearns, R. C.; Paulauskis, J. D.; Godleski, J. J. Endocytosis of Ultrafine Particles by A549 Cells. *Am. J. Respir. Cell Mol. Biol.* **2001**, *24*, 108–115.

12 Rothen-Rutishauser, B. M.; Kiama, S. G.; Gehr, P. A Three-Dimensional Cellular Model of the Human Respiratory Tract to Study the Interaction with Particles. *Am. J. Respir. Cell Mol. Biol.* **2005**, *32*, 281–289.

13 Driscoll, K. E.; Howard, B. W.; Carter, J. M.; Asquith, T.; Johnston, C.; Detilleux, P.; Kunkel, S. L.; Isfort, R. J. Alpha-Quartz-Induced Chemokine Expression by Rat Lung Epithelial Cells: Effects of In Vivo and In Vitro Particle Exposure. *Am. J. Pathol.* **1996**, *149*, 1627–1637.

14 Becher, R.; Hetland, R. B.; Refsnes, M.; Dahl, J. E.; Dahlman, H. J.; Schwarze, P. E. Rat Lung Inflammatory Responses after In Vivo and In Vitro Exposure to Various Stone Particles. *Inhal. Toxicol.* **2001**, *13*, 789–805.

15 Barlow, P. G.; Clouter-Baker, A.; Donaldson, K.; Maccallum, J.; Stone, V. Carbon Black Nanoparticles Induce Type II Epithelial Cells to Release Chemotaxins for Alveolar Macrophages. *Part. Fibre Toxicol.* **2005**, *2*, 11.

16 Merget, R.; Bauer, T.; Kupper, H. U.; Philippou, S.; Bauer, H. D.; Breitstadt, R.; Bruening, T. Health Hazards due to the Inhalation of Amorphous Silica. *Arch. Toxicol.* **2002**, *75*, 625–634.

17 Lee, K. P.; Kelly, D. P. Translocation of Particle-Laden Alveolar Macrophages and Intra-Alveolar Granuloma Formation in Rats Exposed to Ludox Colloidal Amorphous Silica by Inhalation. *Toxicology* **1993**, *77*, 205–222.

18 Warshawsky, D.; Reilman, R.; Cheu, J.; Radike, M.; Rice, C. Influence of Particle Dose on the Cytotoxicity of Hamster and Rat Pulmonary Alveolar Macrophage In Vitro. *J. Toxicol. Environ. Health* **1994**, *42*, 407–421.

19 Johnston, C. J.; Driscoll, K. E.; Finkelstein, J. N.; Baggs, R.; O'Reilly, M. A.; Carter, J.; Gelein, R.; Oberdorster, G. Pulmonary Chemokine and Mutagenic Responses in Rats after Subchronic Inhalation of Amorphous and Crystalline Silica. *Toxicol. Sci.* **2000**, *56*, 405–413.

20 Hetland, R. B.; Schwarze, P. E.; Johansen, B. V.; Myran, T.; Uthus, N.; Refsnes, M. Silica-Induced Cytokine Release from A549 Cells: Importance of Surface Area Versus Size. *Hum. Exp. Toxicol.* **2001**, *20*, 46–55.

21 Singal, M.; Finkelstein, J. N. Amorphous Silica Particles Promote Inflammatory Gene Expression through the Redox Sensitive Transcription Factor, Ap-1, in Alveolar Epithelial Cells. *Exp. Lung. Res.* **2005**, *31*, 581–597.

22 Oberdorster, G.; Ferin, J.; Lehnert, B. E. Correlation between Particle Size, In Vivo Particle Persistence, and Lung Injury. *Environ. Health Perspect* **1994**, *102* (Suppl. 5), 173–179.

23 Donaldson, K.; Beswick, P. H.; Gilmour, P. S. Free Radical Activity Associated with the Surface of Particles: A Unifying Factor in Determining Biological Activity. *Toxicol. Lett.* **1996**, *88*, 293–298.

24 Borm, P.; Klaessig, F. C.; Landry, T. D.; Moudgil, B.; Pauluhn, J.; Thomas, K.; Trottier, R.; Wood, S. Research Strategies for Safety Evaluation of Nanomaterials, Part V: Role of Dissolution in Biological Fate and Effects of Nanoscale Particles. *Toxicol. Sci.* **2006**, *90*, 23–32.

25 Limbach, L. K.; Li, Y.; Grass, R. N.; Brunner, T. J.; Hintermann, M. A.; Muller, M.; Gunther, D.; Stark, W. J. Oxide Nanoparticle Uptake in Human Lung Fibroblasts: Effects of Particle Size, Agglomeration, and Diffusion at Low Concentrations. *Environ. Sci. Technol.* **2005**, *39*, 9370–9376.

26 Takenaka, S.; Karg, E.; Roth, C.; Schulz, H.; Ziesenis, A.; Heinzmann, U.; Schramel, P.; Heyder, J. Pulmonary and Systemic Distribution of Inhaled Ultrafine Silver Particles in Rats. *Environ. Health Perspect.* **2001**, *109* (Suppl. 4), 547–551.

27 Oberdorster, G. Lung Clearance of Inhaled Insoluble and Soluble Particles. *J. Aerosol Med.* **1988**, *1*, 289–329.

28 Heckel, K.; Kiefmann, R.; Dorger, M.; Stoeckelhuber, M.; Goetz, A. E. Colloidal Gold Particles as a New In Vivo Marker of Early Acute Lung Injury. *Am. J. Physiol. Lung Cell Mol. Physiol.* **2004**, *287*, L867–L878.

29 Oberdorster, G. Toxicokinetics and Effects of Fibrous and Nonfibrous Particles. *Inhal. Toxicol.* **2002**, *14*, 29–56.

30 Nemmar, A.; Vanbilloen, H.; Hoylaerts, M. F.; Hoet, P. H.; Verbruggen, A.; Nemery, B. Intratracheally Instilled Ultrafine Particles from the Lung into the Systemic Circulation in Hamster. *Am. J. Respir. Crit. Care Med.* **2001**, *164*, 1665–1668.

31 May, R. C.; Machesky, L. M. Phagocytosis and the Actin Cytoskeleton. *J. Cell. Sci.* **2001**, *114* (Pt. 6), 1061–1077.

32 Conner, S. D.; Schmid, S. L. Regulated Portals of Entry into the Cell. *Nature* **2003**, *422*, 37–44.

33 Schins, R. P.; Duffin, R.; Hohr, D.; Knaapen, A. M.; Shi, T.; Weishaupt, C.; Stone, V.; Donaldson, K.; Borm, P. J. Surface Modification of Quartz Inhibits Toxicity, Particle Uptake, and Oxidative DNA Damage in Human Lung Epithelial Cells. *Chem. Res. Toxicol.* **2002**, *15*, 1166–1173.

34 Kreuter, J. Influence of The Surface Properties on Nanoparticle-Mediated Transport of Drugs to the Brain. *J. Nanosci. Nanotechnol.* **2004**, *4*, 484–488.

35 Lorenz, M. R.; Holzapfel, V.; Musyanovych, A.; Nothelfer, K.; Walther, P.; Frank, H.; Landfester, K.; Schrezenmeier, H.; Mailander, V. Uptake of Functionalized, Fluorescent-Labeled Polymeric Particles in Different Cell Lines and Stem Cells. *Biomaterials* **2006**, *27*, 2820–2828.

36 Donaldson, K.; Stone, V.; Duffin, R.; Clouter, A.; Schins, R.; Borm, P. The Quartz Hazard: Effects of Surface and Matrix on Inflammogenic Activity. *J. Environ. Pathol. Toxicol. Oncol.* **2001**, *20* (Suppl. 1), 109–118.

37 Fubini, B.; Fenoglio, I.; Ceschino, R.; Ghiazza, M.; Martra, G.; Tomatis, M.; Borm, P.; Schins, R.; Bruch, J. Relationship Between the State of the Surface of Four Commercial Quartz Flours and their Biological Activity in Vitro and In Vivo. *Int. J. Hyg. Environ. Health* **2004**, *207*, 89–104.

38 Xia, T.; Kovochich, M.; Brant, J.; Hotze, M.; Sempf, J.; Oberley, T.; Sioutas, C.; Yeh, J. I.; Wiesner, M. R.; Nel, A. E. Comparison of the Abilities of Ambient and Manufactured Nanoparticles to Induce Cellular Toxicity According to an Oxidative Stress Paradigm. *Nano. Lett.* **2006**, *6*, 1794–1807.

39 Welch, M. D.; Mallavarapu, A.; Rosenblatt, J.; Mitchison, T. J. Actin Dynamics In Vivo. *Curr. Opin. Cell. Biol.* **1997**, *9*, 54–61 (Review).

40 Medeiros, N. A.; Burnette, D. T.; Forscher, P. Myosin II Functions in Actin-Bundle Turnover in Neuronal Growth Cones. *Nat. Cell Biol.* **2006**, *8*, 215–226.

41 Smith, G. J.; Lykke, A. W. Characterization of a Neoplastic Epithelial Cell Strain Derived by Dexamethasone Treatment of Cultured Normal Mouse Type 2 Pneumocytes. *J. Pathol.* **1985**, *147*, 165–172.

42 Malkinson, A. M.; Dwyer-Nield, L. D.; Rice, P. L.; Dinsdale, D. Mouse Lung Epithelial Cell Lines—Tools for the Study of Differentiation and the Neoplastic Phenotype. *Toxicology* **1997**, *123*, 53–100.

43 Orr, G.; Hu, D.; Ozcelik, S.; Opresko, L. K.; Wiley, H. S.; Colson, S. D. Cholesterol Dictates the Freedom of EGF Receptors and HER2 in the Plane of the Membrane. *Biophys. J.* **2005**, *89*, 1362–1373.

44 Hoet, P. H.; Bruske-Hohlfeld, I.; Salata, O. V. Nanoparticles—Known and Unknown Health Risks. *J. Nanobiotechnol.* **2004**, *2*, 12.

45 Tani, T.; Miyamoto, Y.; Fujimori, K. E.; Taguchi, T.; Yanagida, T.; Sako, Y.; Harada, Y. Trafficking of a Ligand-Receptor Complex on the Growth Cones as an Essential Step for the Uptake of Nerve Growth Factor at the Distal End of the Axon: A Single-Molecule Analysis. *J. Neurosci.* **2005**, *25*, 2181–2191.

46 Lidke, D. S.; Lidke, K. A.; Rieger, B.; Jovin, T. M.; Arndt-Jovin, D. J. Reaching out for Signals: Filopodia Sense EGF and Respond by Directed Retrograde Transport of Activated Receptors. *J. Cell. Biol.* **2005**, *170*, 619–626.

47 Gottlieb, T. A.; Ivanov, I. E.; Adesnik, M.; Sabatini, D. D. Actin Microfilaments Play a Critical Role in Endocytosis at the Apical but not the Basolateral Surface of Polarized Epithelial Cells. *J. Cell. Biol.* **1993**, *120*, 695–710.

48 Shurety, W.; Bright, N. A.; Luzio, J. P. The Effects of Cytochalasin D and Phorbol Myristate Acetate on the

Apical Endocytosis of Ricin in Polarised Caco-2 Cells. *J. Cell. Sci.* **1996**, *109* (Pt. 12), 2927–2935.
49 Lehmann, M. J.; Sherer, N. M.; Marks, C. B.; Pypaert, M.; Mothes, W. Actin- and Myosin-Driven Movement of Viruses along Filopodia Precedes their Entry into Cells. *J. Cell. Biol.* **2005**, *170*, 317–325.
50 Mislick, K. A.; Baldeschwieler, J. D. Evidence for the Role of Proteoglycans in Cation-Mediated Gene Transfer. *Proc. Natl. Acad. Sci. U.S.A.* **1996**, *93*, 12349–12354.
51 Freissler, E.; Meyer auf der Heyde, A.; David, G.; Meyer, T. F.; Dehio, C. Syndecan-1 and Syndecan-4 can Mediate the Invasion of Opahspg-Expressing Neisseria Gonorrhoeae into Epithelial Cells. *Cell. Microbiol.* **2000**, *2*, 69–82.
52 Jeng, R. L.; Welch, M. D. Cytoskeleton: Actin and Endocytosis—No Longer the Weakest Link. *Curr. Biol.* **2001**, *11*, R691–R694 (Review).
53 Yarar, D.; Waterman-Storer, C. M.; Schmid, S. L. A Dynamic Actin Cytoskeleton Functions at Multiple Stages of Clathrin-Mediated Endocytosis. *Mol. Biol. Cell* **2005**, *16*, 964–975.
54 Teeguarden, J. G.; Hinderliter, P. M.; Orr, G.; Thrall, B. D.; Pounds, J. G. Particokinetics In Vitro: Dosimetry Considerations for In Vitro Nanoparticle Toxicity Assessments. *Toxicol. Sci.* **2007**, *95*, 300–312.
55 Gelles, J.; Schnapp, B. J.; Sheetz, M. P. Tracking Kinesin-Driven Movements with Nanometre-Scale Precision. *Nature* **1988**, *331*, 450–453.